A multiscale poromechanics model integratingmyocardial perfusion and systemic circulation

Barnafi, N.; Di Gregorio, S.; Dede', L.; Zunino, P.; Vergara, C.;

Quarteroni, A.

A multiscale poromechanics model integrating myocardial perfusion and systemic circulation

Nicolás A. Barnafi[†]   Simone Di Gregorio[♯]   Luca Dede'[♯]

Paolo Zunino[♯]   Christian Vergara[⋆]   Alfio Quarteroni[♯ ♭]

June 14, 2021

[†] Dipartimento di Matematica "F. Enriques"
Università degli Studi di Milano
Milan, Italy
nicolas.barnafi@unimi.it

[♯] MOX– Modellistica e Calcolo Scientifico
Dipartimento di Matematica "F. Brioschi"
Politecnico di Milano
Milan, Italy
{simone.digregorio,luca.dede,paolo.zunino,alfio.quarteroni}@polimi.it

[⋆] Laboratory of Biological Structure Mechanics (LaBS)
Dipartimento di Chimica, Materiali e Ingegneria Chimica "Giulio Natta"
Politecnico di Milano
Milan, Italy
christian.vergara@polimi.it

[♭] Chair of Modelling and Scientific Computing (CMCS)
École polytechnique fédérale de Lausanne
Lausanne, Switzerland
alfio.quarteroni@epfl.ch

1

Abstract

The importance of myocardial perfusion at the outset of cardiac disease remains largely understudied. To address this topic we present a mathematical model that considers the systemic circulation, the coronary vessels, the myocardium, and the interactions among these components. The core of the whole model is the description of the myocardium as a multi-compartment poromechanics system. A novel decomposition of the poroelastic Helmholtz potential involved in the poromechanics model allows for a quasi-incompressible model that adequately describes the physical interaction among all components in the porous medium. We further provide a rigorous mathematical analysis that gives guidelines for the choice of the Helmholtz potential. To reduce the computational cost of our integrated model we propose decoupling the deformation of the tissue and systemic circulation from the porous flow in the myocardium and coronary vessels, which allows us to apply the model also in combination with pre-computed cardiac displacements, obtained form other models or medical imaging data. We test the methodology through the simulation of a heartbeat in healthy conditions that replicates the systolic impediment phenomenon, which is particularly challenging to capture as it arises from the interaction of several parts of the model.

1 Introduction

Cardiac perfusion is the blood supply of the heart muscle and it involves three components. The first one is the *cardiac tissue*, known as myocardium. The second one is the *coronary vasculature*, which carries blood from the aorta to the myocardium and then to the venous system, and it is composed by two parts: the epicardial coronary vessels, stemming from the aorta and embracing the heart, and the myocardial coronary vessels (also known as intramural coronary vessels or coronary microvasculature), carrying the blood in the tissue to the venous system. The third component is the *systemic circulation*, which carries blood to the rest of the organs. The myocardial coronary vessels present large variations of spatial scales in the range of 10–500 μm [DJBBD92, FAC16] with very different mechanical properties [AKL10a] and a complex network structure [HBRS08, LMR+10, LS12]. As a result, the pressure that drives perfusion in the coronary microvasculature is given by the combined effects of the intra-vessel and intra-myocardial pressures [AKL10b].

Mathematical models have been widely used to study this problem. The complex multi-scale nature of the coronary microvasculature and its interaction with the myocardium has been mainly addressed by the use of poromechanics models [HAvCR92, VSW97, Smi04, CGSMVC10, CLM+12, VYW15, PKJ+20], consisting in a continuum model [Cou04] obtained by a formal averaging of the fluid porous structure (vessels) and the solid phase (myocardium) [Whi86]. This approach does not necessitate a detailed geometric description of the vessels, which would be impossible to obtain from medical imaging *in-vivo* and, in any

case, computationally untractable. A more accurate description can be given by multi-compartment formulations, wherein a scale separation procedure allows to consider different vessel resolutions separately (e.g. arterioles, capillaries, venules) [CLM$^+$12, MCC$^+$13, DGFP$^+$20].

Epicardial coronary vessels can be modeled either in full 3D resolution [KVCC$^+$10, DGFP$^+$20] or by means of reduced models, which can be either lumped (namely zero-dimensional, 0D, models) [WBDVN69, QRV01, FQV09, DK75, HS90, KCB85, NLL$^+$20] or one-dimensional (1D) [BB00, HKL$^+$09, LNN$^+$09, NKL18]. The main advantage of 1D models with respect to 0D ones is the ability to capture wave propagation phenomena, particularly relevant in the coronary blood dynamics [GPCP90]. Finally, systemic circulation has been often modeled as a network of 0D elements, based on RLC elements [QVV16] and Windkessel models [WLW09] considering separately the lungs (supplied by right ventricle) from the rest of the body [BF10, HBJ$^+$17] (supplied by the left ventricle).

The scope of our work is the creation of a new mathematical model of cardiac perfusion encompassing all of the aforementioned components and their interactions, whose layout is shown in Figure 1. The interaction between the intramural coronary vessels and the heart tissue is described employing a multi-compartment poromechanics model. One distinctive feature of our new model is the use of a quasi-incompressible formulation, achieved by combining the Helmholtz potential from [CLM$^+$12] with the thermodynamically motivated energy presented in [CM14]. This combination yields a better representation of the underlying physics and, most importantly, the pressure in the coronary microvasculature results as the difference between the intra-vessel and intra-myocardial pressures in each compartment. Our proposed poroelastic Helmholtz potential presents two further advantages: i) it enables the straightforward use of constitutive laws already available in the literature and, ii) it provides analytic conditions that guarantee the existence of solutions for each of the problems within the poromechanics model, namely the mechanics and porous media equations.

Regarding blood flow in the epicardial coronaries, we consider a 0D model [QRV01, FQV09], where we generalize the standard formulation to make it better suited for arbitrary networks of vessels. Finally, we consider an additional 0D model for the circulatory system that yields a closed loop of blood flow through the body [RSA$^+$20a, RSA$^+$20b].

For the numerical approximation, we neglect the feedback of blood pressure on both the circulatory system and the heart mechanics. This results in a one-way coupling strategy that allows our model to be used with a prescribed myocardial displacement obtained either by an electromechanics simulation or prescribed from imaging techniques [CWH$^+$16], with the additional advantage of greatly reducing computational costs.

This paper is structured as follows: in Section 2 we present the poromechanics model for the myocardium and the novel constitutive law, in Section 3 we introduce the generalized 0D coronary vessel model, in Section 4 we present the coupled perfusion model together with the one-way coupling hypothesis and in

3

Section 5 we perform a realistic numerical simulation to validate the proposed model.
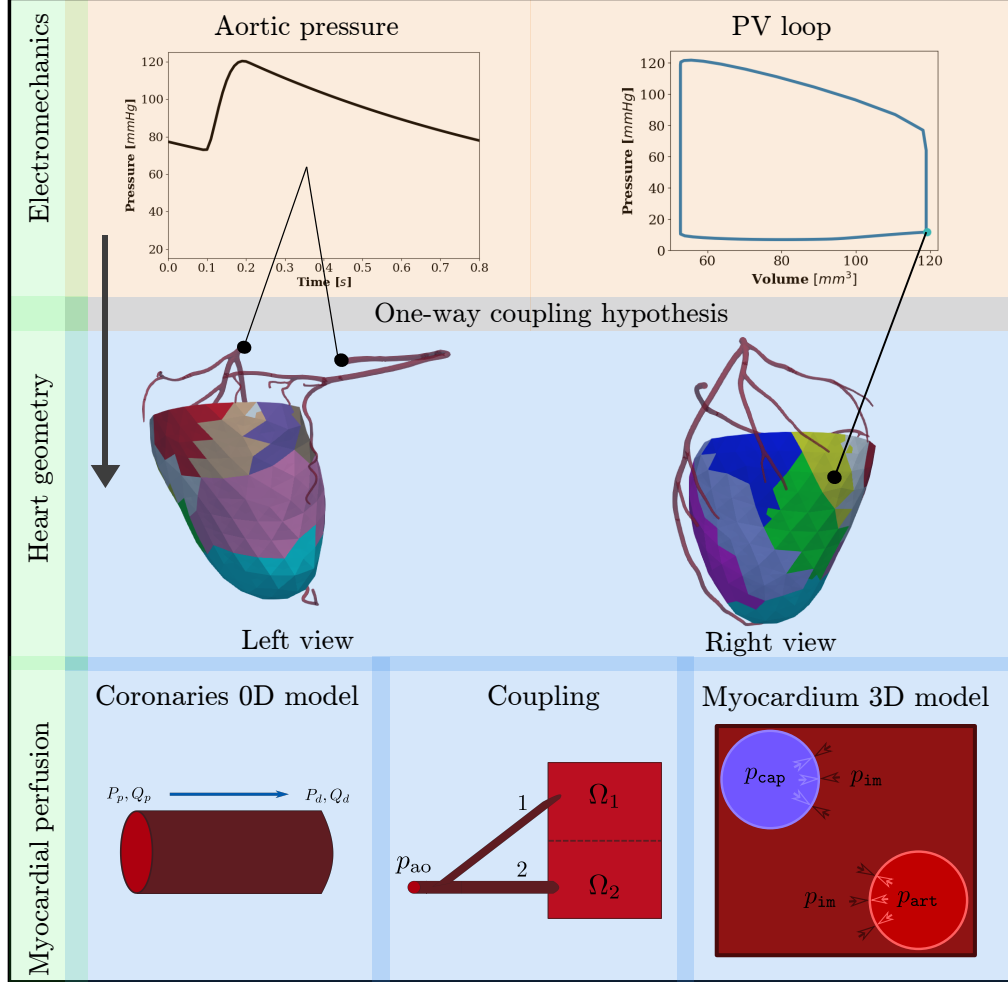

Figure 1: Description of the general layout of the integrated perfusion model and of the coupling with the heart contraction for the application to myocardial perfusion. In 'Coupling', p_{ao} stands for the aortic pressure and Ω_1, Ω_2 represent those regions perfused by vessels 1 and 2 respectively. In 'Myocardium 3D model', p_{cap}, p_{art} and p_{im} stand for the capillary, arterial and intra-myocardial pressures respectively.

2 Mathematical model for the myocardium and intramural coronary vessels

In this section we propose a novel constitutive model for poromechanics. This is achieved by considering the energy contribution of the local volumes of the solid [dBCD98, CM14], the fluid phases [CLM+12] and the total volume (as in quasi-incompressible mechanics). The resulting energy yields a quasi-incompressible model that is very convenient for numerical simulations.

2.1 Poromechanics with large deformations

We review the balance laws for poromechanics by following [CM14]. For this, consider a reference domain Ω_0, deformed at time t into $\Omega(t)$ where possibly $\Omega_0 \neq \Omega(0)$. Deformation is given by a map $\boldsymbol{x}_t : \Omega_0 \to \Omega(t)$, and we use the standard notation that $\boldsymbol{x} := \boldsymbol{y}_s + \boldsymbol{X}$, so that $\boldsymbol{x}$ is the *current* coordinate, $\boldsymbol{X}$ is the *reference* coordinate and $\boldsymbol{y}_s$ is the displacement. We also define the strain tensor $\boldsymbol{F} := \nabla_{\boldsymbol{X}} \boldsymbol{y}_s$, its determinant $J := \det \boldsymbol{F}$ and the solid velocity $\boldsymbol{v}_s := \frac{\partial \boldsymbol{y}_s}{\partial t}$.

Poromechanics is a mixture theory [Bow80, Bow82], which means that the domain of interest is composed by coexisting phases. If we consider N_C fluid types (or compartments) and one solid phase, we can formally define a fluid volume fraction as $\phi_i := \frac{d\Omega_{\text{fluid}_i}(t)}{d\Omega(t)}$ named *porosity*, where $d\Omega_{\text{fluid}_i}$ represents the differential volume of compartment i, and a solid volume fraction $\phi_s := 1 - \sum_{i=1}^{N_C} \phi_i$. These quantites relate the phase measure to the Lebesgue measure through $d\Omega_{\text{fluid}_i(t)} = \phi_i d\Omega(t)$. Their reference counterpart, i.e. the Lagrangian porosities given by $\varphi_i := J\phi_i$, are the primary variables regarding mass conservation. The initial and solid Lagrangian porosities are then given by $\varphi_{i,0} = J_0\phi_{i,0}$ and $\varphi_s = J - \sum_{i=1}^{N_C} \varphi_i$ respectively.

Mass conservation   We consider a compartment $i \in \{1, ..., N_C\}$, a distributed mass source term θ_i associated to the fluid phase, and define the fluid, solid and total densities as $\rho_{f,i}, \rho_s$ and $\rho := \phi_s \rho_s + \sum_{i=1}^{N_C} \phi_i \rho_{f,i}$ respectively.

We additionally define the reference density of added mass m_i in Ω_0 as the difference between the fluid content in current and initial configurations, $m_i := \rho_{f,i}(\varphi_i - \varphi_0)$, with which we obtain mass conservation in each compartment i as

$$\frac{dm_i}{dt} + \text{div}_{\boldsymbol{X}}(\boldsymbol{W}_i) = \Theta_i - J\sum_{j=1}^{N_C} \beta_{ij}(p_i - p_j) \quad \text{in} \quad \Omega_0, \tag{1}$$

where $\Theta_i := J\theta_i$ is the reference source term for a current distributed mass source θ_i, $\boldsymbol{W}_i := \rho_{f,i}\phi_i \boldsymbol{V}_{r,i}$ is the reference flow vector, $\boldsymbol{V}_{r,i} := J\boldsymbol{F}^{-1}(\boldsymbol{v}_{f,i} - \boldsymbol{v}_s)$ is the reference relative velocity, β_{ij} is an inter-compartment interaction coefficient and pressure is obtained through constitutive modeling from a Helmholtz potential Ψ as $p_i = \frac{\partial \Psi}{\partial \varphi_i}$. We note that the added mass density m_i and Lagrangian porosity

5

φ_i are related by an affine transformation, so both are valid candidates for being primary variables. Still, the Lagrangian porosity is preferable as it is dimensionless and, as seen from the definition of the pressure, it is also the natural thermodynamic quantity of this model.

The flow vector can be obtained from the pressure gradient through a Darcy law by means of a permeability tensor $\tilde{\boldsymbol{k}}_{f,i}$, given by

$$\boldsymbol{W}_i = -\rho_{f,i} J \boldsymbol{F}^{-1} \tilde{\boldsymbol{k}}_{f,i} \boldsymbol{F}^{-T} \nabla_{\boldsymbol{X}} p_i = -\rho_{f,i} \boldsymbol{K}_{f,i} \nabla_{\boldsymbol{X}} p_i, \tag{2}$$

where we defined the Lagrangian permeability tensor $\boldsymbol{K}_{f,i} := J \boldsymbol{F}^{-1} \tilde{\boldsymbol{k}}_{f,i} \boldsymbol{F}^{-T}$. We consider a no-slip boundary condition, given by

$$\boldsymbol{W}_i \cdot \boldsymbol{n} = -\rho_{f,i} \boldsymbol{K}_{f,i} \nabla_{\boldsymbol{X}} p_i = 0 \quad \text{on} \quad \partial\Omega_0.$$

Conservation of momentum We consider the standard conservation of momentum in quasi-static form, given by

$$-\operatorname{div}_{\boldsymbol{X}} \boldsymbol{P}_{\text{tot}} = \boldsymbol{0} \qquad \text{in} \quad \Omega_0, \tag{3}$$

where $\boldsymbol{P}_{\text{tot}}$ is the total Piola stress tensor. In cardiac modeling, the stress tensor considers both passive and active mechanics, so we adopt an active stress approach [QLRRB17, AANQ11] which yields $\boldsymbol{P}_{\text{tot}} = \boldsymbol{P} + \boldsymbol{P}_a$, where $\boldsymbol{P}_a$ models the active mechanics and $\boldsymbol{P}$, obtained from constitutive modeling as $\boldsymbol{P} = \frac{\partial \Psi}{\partial \boldsymbol{F}}$, models the passive mechanics. For the boundary, we consider a Robin condition which accounts for the friction with the pericardium and the effect of the atra at the base [ULM02]:

$$\boldsymbol{P}_{\text{tot}} \boldsymbol{n} + k_\perp \boldsymbol{f}_0 \otimes \boldsymbol{f}_0 \boldsymbol{y}_s + 0.1 k_\perp (\boldsymbol{I} - \boldsymbol{f}_0 \otimes \boldsymbol{f}_0) \boldsymbol{y}_s = 0 \qquad \text{on} \quad \partial\Omega_0, \tag{4}$$

where $k_\perp = 2 \, 10^5 \, \text{Pa}$ [PHW+19]. We denote it by $\boldsymbol{P}_{\text{tot}} \boldsymbol{n} = \boldsymbol{g}(\boldsymbol{y}_s)$ on Ω_0. The active stress term is given by a fiber-oriented force:

$$\boldsymbol{P}_a(\boldsymbol{F}, t) = \gamma(t) \frac{(\boldsymbol{F} \boldsymbol{f}_0) \otimes \boldsymbol{f}_0}{|\boldsymbol{F} \boldsymbol{f}_0|},$$

where $\boldsymbol{f}_0$ represents a fiber orientation and γ, possibly also space dependent, represents the activation of the cardiomyocites (heart muscle cells), driven by the heart's electrophysiology. Further details on these topics can be found in [BBPT12] and [FPS14] respectively.

The multicompartment model In what follows, we consider all quantities in reference configuration and thus drop the subindex from differential operators as $\nabla = \nabla_{\boldsymbol{X}}, \operatorname{div} = \operatorname{div}_{\boldsymbol{X}}$. Putting everything together, the multi-compartment poromechanics model is given by: Find a displacement $\boldsymbol{y}_s$ and Lagrangian porosities $\boldsymbol{\varphi} = (\varphi_1, ..., \varphi_{N_C})$ such that for each $t > 0$ it holds that

$$-\operatorname{div}(\boldsymbol{P}(\boldsymbol{F},\boldsymbol{\varphi}) + \boldsymbol{P}_a(\boldsymbol{F})) = \boldsymbol{0} \qquad \text{in} \quad \Omega_0, \tag{5a}$$

$$\frac{d\varphi_i}{dt} - \operatorname{div}\left(\boldsymbol{K}_i(\boldsymbol{F})\nabla_{\boldsymbol{X}}p_i(\boldsymbol{F},\boldsymbol{\varphi})\right) \tag{5b}$$

$$+ \sum_{j=1}^{N_C} \beta_{ij}(p_i(\boldsymbol{F},\boldsymbol{\varphi}) - p_j(\boldsymbol{F},\boldsymbol{\varphi})) = J\theta_i \qquad \text{in} \quad \Omega_0, \quad \forall i \in \{1,...,N_C\},$$

$$(\boldsymbol{P} + \boldsymbol{P}_a)\boldsymbol{n} = \boldsymbol{g}(\boldsymbol{y}_s) \qquad \text{on} \quad \partial\Omega_0, \tag{5c}$$

$$\rho_{f,i}\boldsymbol{K}_{f,i}(\boldsymbol{F})\nabla p \cdot \boldsymbol{n} = 0 \qquad \text{on} \quad \partial\Omega_0, \quad \forall i \in \{1,...,N_C\}, \tag{5d}$$

$$\boldsymbol{\varphi}(0) = \boldsymbol{\varphi}_0 \qquad \text{in} \quad \Omega_0. \tag{5e}$$

2.2 Constitutive modeling

In nonlinear poroelasticity with incompressible fluids, the Piola stress tensor $\boldsymbol{P}$ and the compartment pressures p_i for $i \in \{1,...,N_C\}$ are obtained from a Helmholtz potential Ψ [Cou04, CLM$^+$12]:

$$\boldsymbol{P}(\boldsymbol{F},\boldsymbol{\varphi}) = \frac{\partial\Psi}{\partial\boldsymbol{F}}(\boldsymbol{F},\boldsymbol{\varphi}), \quad p_i(\boldsymbol{F},\boldsymbol{\varphi}) = \frac{\partial\Psi}{\partial\varphi_i}(\boldsymbol{F},\boldsymbol{\varphi}). \tag{6}$$

The main approaches for constitutive modeling in cardiac poromechanics are based on additive splittings of the Helmholtz potential Ψ. In what follows, we present a brief review of such models to motivate the proposal of a new one which yields fully quasi-incompressible poromechanics, i.e. without the imposition of incompressibility constraints on any of the phases involved.

Additive splitting with fluid porosity [CLM$^+$12] This approach decomposes the energy into skeleton and fluid parts. This is achieved by considering one potential for the solid phase ψ_{skel} and one for each fluid compartment ψ_i as

$$\Psi_A(\boldsymbol{F},\boldsymbol{\varphi}) = \psi_{\text{skel}}(\boldsymbol{F}) + \sum_{i=1}^{N_C} \psi_i(\varphi_i), \tag{7}$$

which does not account for the interaction between the porous media and the mechanics. This limitation is circumvented in [CLM$^+$12] by the use of a Lagrange multiplier λ with respect to the incompressibility of the solid phase $J = J_0 + \sum_{i=1}^{N_C} m_i/\rho_f$, so the modified energy yields

$$\boldsymbol{P}(\boldsymbol{F},\boldsymbol{\varphi}) = \frac{\partial\psi_{\text{skel}}}{\partial\boldsymbol{F}}(\boldsymbol{F}) - \lambda J\boldsymbol{F}^{-T}, \quad p_i(\boldsymbol{F},\boldsymbol{\varphi}) = \frac{\partial\psi_i}{\partial\varphi_i}(\varphi_i) + \lambda.$$

This indeed allows for the recovery of the interaction between physics, but adds two difficulties. On one side, a constrained problem results in a saddle point problem that is in general more difficult to approximate numerically. On the

other side, there is lack of control on λ from the modeling point of view which makes it difficult to model the pressure response due to deformation. In addition, the functions ψ_i are such that $\lim_{\varphi_i \to 0} \psi_i(\varphi_i) = \infty$ and so $\phi_i > 0$ for all $i \in \{1, ..., N_C\}$, but do not guarantee that $\sum_{j=1}^{N_C} \phi_j < 1$.

Additive splitting with solid porosity [CM14] This approach, based on [dBCD98], considers a decomposition of the energy into a skeleton part and a solid porosity part. It reads

$$\Psi_B(\boldsymbol{F}, \varphi) = \psi_{\text{skel}}(\boldsymbol{F}) + \psi_s(\varphi_s), \tag{8}$$

and it depends only on the solid porosity. This formulation captures the feedback of the skeleton on the fluid and vice-versa:

$$\boldsymbol{P}(\boldsymbol{F}, \boldsymbol{\varphi}) = \frac{\partial \psi_{\text{skel}}}{\partial \boldsymbol{F}}(\boldsymbol{F}) + \frac{\partial \psi_s}{\partial \varphi_s}(\varphi_s) J \boldsymbol{F}^{-T}, \quad p_i(\boldsymbol{F}, \boldsymbol{\varphi}) = -\frac{\partial \psi_s}{\partial \varphi_s}(\varphi_s), \tag{9}$$

but it presents two drawbacks. The first one is that the pressure expression is the same for each compartment i, and the second one is that the resulting problem is degenerate parabolic, with no control over the single compartment. To see the last point, we consider only mass conservation (14) on each compartment, with $\boldsymbol{K} = \boldsymbol{I}$, $\rho_f = 1$, no compartment interaction ($\beta_{ik} = 0$) and no source term ($\Theta_i = 0$). Thus we can recast the mass conservation in the i-th compartment as

$$\frac{\partial \varphi_i}{\partial t} + \text{div}\left(\frac{\partial p}{\partial \varphi_s} \nabla \varphi_s \right) = 0,$$

where we used $\nabla p = \frac{\partial p}{\partial \varphi_s} \nabla \varphi_s$. If we assume that the potential ψ_s is strictly convex with $\frac{\partial^2 \psi_s}{\partial \varphi_s^2} \geq \psi_0 > 0$, then by testing each equation by a test function q_i in $H_0^1(\Omega_0)$, denoting the L^2 inner product with $(\cdot, \cdot)$ and focusing only on the differential operator, we see that the problem is degenerate parabolic, as we obtain control only on the sum of the (fluid) porosities:

$$\left(\frac{\partial^2 \psi_s}{\partial \varphi_s^2} \left(\sum_{i=1}^{N_c} \nabla \varphi_i \right), \left(\sum_{i=1}^{N_c} \nabla \varphi_i \right) \right) \geq \psi_0 \left\| \sum_{i=1}^{N_c} \nabla \varphi_i \right\|_{L^2(\Omega_0)}^2$$

for all $\varphi_i \in H^1(\Omega_0)$. In contrast to the previous model, this one yields $\phi_s(\varphi_s) \to \infty$ as $\phi_s \to 1$ and thus guarantees $\sum_{j=1} \phi_j < 1$, but it fails to enforce $\phi_i > 0$ for all $i \in \{1, ..., N_C\}$.

In what follows we propose a new strategy for devising a poroelastic potential Ψ, that overcomes the disadvantages of the previous ones.

New additive splitting with fluid and solid porosities We consider a new decomposition that combines the previous approaches:

$$\Psi(\boldsymbol{F}, \boldsymbol{\varphi}) = \overbrace{\psi_{\text{skel}}(\boldsymbol{F}) + \underbrace{\psi_s(\varphi_s)}^{\text{mechanics}} + \sum_{i=1}^{N_C} \psi_i(\varphi_i)}_{\text{porous media}} .$$

This gives the relations

$$\boldsymbol{P}(\boldsymbol{F}, \boldsymbol{\varphi}) = \frac{\partial \psi_{\text{skel}}}{\partial \boldsymbol{F}}(\boldsymbol{F}) + \frac{\partial \psi_s(\varphi_s)}{\partial \varphi_s} J \boldsymbol{F}^{-T}, \quad p_i(\boldsymbol{F}, \boldsymbol{\varphi}) = \frac{\partial \psi_i}{\partial \varphi_i}(\varphi_i) - \frac{\partial \psi_s}{\partial \varphi_s}(\varphi_s), \quad (10)$$

from which we highlight the following aspects:

1. The porous part $\psi_s + \sum_i \psi_i$ acts as a double barrier potential constraining the porosity such that $0 < \phi_i$ for all $i \in \{1, ..., N_C\}$ and $\sum_{j=1}^{N_C} \phi_j < 1$.

2. The pressure-like term $\frac{\partial \psi_s(\varphi_s)}{\partial \varphi_s} J \boldsymbol{F}^{-T}$ appearing in the Piola stress tensor is driven by the pressure in the solid portion of the tissue φ_s only.

3. The pressure acting on the blood is the difference between the one in the compartment (luminar) and the one in the tissue (intramyocardial). It is known as transmural pressure and is correctly captured from the proposed potential:

$$p_i(\boldsymbol{F}, \boldsymbol{\varphi}) = \underbrace{\frac{\partial \psi_i}{\partial \varphi_i}(\varphi_i)}_{\text{luminar pressure}} - \underbrace{\frac{\partial \psi_s}{\partial \varphi_s}(\varphi_s)}_{\text{intramyocardial pressure}} .$$

Remark 2.1 *The potential ψ_s yields a similar interaction to that of the Lagrange multiplier λ used in the model of additive splitting with fluid porosity. In fact, the multiplier imposes the constraint $\varphi_s - (J_0 - \sum_i \varphi_{i,0}) = 0$, which is the quantity penalized by the potential ψ_s.*

2.3 Constitutive model used for cardiac perfusion

We present expressions for $\psi_{\text{skel}}, \psi_s$ and $\psi_i, i = 1, \ldots, N_C$ defined in Section 2.2, which are adequate for cardiac poromechanics. We highlight that the proposed constitutive model allows for all energy terms to be obtained from existing literature.

Skeleton energy We consider a Guccione constitutive law [GMW91], given by

$$\psi_{\text{skel}}(\boldsymbol{F}) = C \exp\{Q(\boldsymbol{F}) - 1\} + \frac{\kappa}{2}(J - 1) \log J,$$

$$Q = b_f E_{ff}^2 + b_s E_{ss}^2 + b_n E_{nn}^2 + 2(b_{fs} E_{fs}^2 + b_{fn} E_{fn}^2 + b_{sn} E_{sn}^2),$$

$$\boldsymbol{E} = \frac{1}{2}(\boldsymbol{F}^T \boldsymbol{F} - \boldsymbol{I}), \boldsymbol{F} = \nabla \boldsymbol{y}_s + \boldsymbol{I}, E_{uv} = (\boldsymbol{E} \boldsymbol{v}) \cdot \boldsymbol{u},$$

where $\boldsymbol{f}, \boldsymbol{s}$ and $\boldsymbol{n}$ are a pointwise set of independent vectors directed towards the heart fibers, sheets and normal directions.

Solid phase energy The term ψ_s represents a penalization on the solid Langrangian porosity φ_s. Its role is similar to that of the quasi-incompressibility term included in ψ_{skel}, and for it we adapt the expression used in [BCM17]:

$$\psi_s = \kappa_s \left(\varphi_s - \varphi_{s0} - \log\left(\frac{\varphi_s}{\varphi_{s0}}\right) \right).$$

Fluid phases energy Functional relations between pressure and intramural vessel volume have been proposed in [BADS88] and were obtained by fitting (real) data. In [BADS88], such laws were proposed for a three-compartment 0D model of the heart composed of (myocardial coronary) arteries, capillaries and veins, which makes it a perfect candidate for our multi-compartment framework. Such laws, although devised to represent the coronary pressure, present no dependence on the myocardium (i.e. φ_s), so we consider them instead as the fluid compartment energies. This results in the following relationship for each compartment i:

$$\psi_i(\varphi_i) = c_{i,1} \exp(c_{i,3}\varphi_i) + c_{i,2} \log(c_{i,3}\varphi_i). \tag{11}$$

Pre-stress and myocardial pressure The reference configuration given by the null displacement $\Omega_0 := \Omega(\boldsymbol{0})$ is most probably not in equilibrium when considering the inner stresses and the blood pressure in the heart chambers. This has motivated the computation of an initial configuration $\Omega(\boldsymbol{y}_{s0})$ known as *pre-stress* configuration which is in mechanic equilibrium [HB11, GDQ19, DGQ20], and is usually associated to the end of diastole. We propose extending the same principle to the compartment pressure p_i, meaning that the pre-stress configuration is in pressure equilibrium in each compartment. This can be achieved by rescaling the pressure laws with respect to reference pressures $p_{\text{ref,i}}$. For this, we denote the pre-stress displacement and initial Lagrangian porosities as $\boldsymbol{y}_{s0}$ and $\boldsymbol{\varphi}_0$ respectively and impose that $p_i(\boldsymbol{F}_0, \boldsymbol{\varphi}_0) = p_{\text{ref,i}}$, which results in a rescaled pressure $\tilde{p}_i$:

$$\tilde{p}_i(\boldsymbol{F}, \boldsymbol{\varphi}) = p_i(\boldsymbol{F}, \boldsymbol{\varphi}) - p_i(\boldsymbol{F}_0, \boldsymbol{\varphi}_0) + p_{\text{ref,i}}.$$

Note that this is an intra-compartment balance, as flow between compartments is still possible if there is a pressure difference between them.

2.4 Mathematical properties of the poromechanics model

The mathematical analysis of problem (5) is still open. System (5) consists in the coupling of two well-known problems: the nonlinear quasi-static mechanics (5a) and the porous media equation (5b), which pose well established regularity requirements on the form of the Helmholtz potential Ψ. In this section, in view of

the well posedness analysis, we: i) ignore the Robin condition (4) and consider a homogeneous Dirichlet boundary condition on $\partial\Omega$, ii) disregard the active stress, i.e. $P_a = 0$ and iii) consider a mono-compartment system ($N_C = 1$) with $\boldsymbol{K}_f = \boldsymbol{I}/(J\rho_f), \rho_f = 1$ and $\Theta_1 = 0$. We study both sub-problems, mechanics and porous media, separately.

The mechanics subproblem We first observe that problem (5a) can be reformulated as a minimization problem: given a function φ, find a minimizer $\boldsymbol{y}_s$ of

$$\min_{\boldsymbol{y}_s \in \mathbf{W}} \int_{\Omega} \Psi_S(\boldsymbol{F}, \varphi) \, dX, \tag{12}$$

where $\mathbf{W} = \{\boldsymbol{y}_s{}^* \in \boldsymbol{W}^{1,1}(\Omega) : \boldsymbol{P}(\boldsymbol{F}(\boldsymbol{y}_s{}^*))\boldsymbol{n} = \boldsymbol{g}(\boldsymbol{y}_s{}^*) \text{ on } \partial\Omega_0, \Psi_S(\boldsymbol{y}_s{}^*) < \infty\}$. Existence of minimizers of problem (12) can be established in virtue of the following well-known result [MQY94], which we adapted to consider the dependence on φ.

Theorem 2.1 *For every Lagrangian porosity φ assume the following hypotheses hold:*

$(HS)_1$ Ψ_S *is polyconvex, so there exists a convex function G_φ defined in $\mathbb{R}^d \times \mathbb{R}^d \times \mathbb{R}$ such that*

$$\Psi_S(\boldsymbol{F}, \varphi) = G_\varphi(\boldsymbol{F}, \operatorname{cof} \boldsymbol{F}, \det \boldsymbol{F}), \tag{13}$$

where $\operatorname{cof} \boldsymbol{F} = \det(\boldsymbol{F})\boldsymbol{F}^{-T}$.

$(HS)_2$ Ψ_S *is a Carathéodory function, i.e. $\boldsymbol{F} \to \Psi_S(\boldsymbol{X}, \boldsymbol{F}, \varphi)$ is continuous and $\boldsymbol{X} \to \Psi_S(\boldsymbol{X}, \boldsymbol{F}, \varphi)$ is measurable with $\Psi_S = \infty$ if and only if $J \leq 0$.*

$(HS)_3$ Ψ_S *is coercive, meaning that there exist constants $a > 0, p \geq 2, q \geq 3/2$ such that*

$$\Psi_S(\boldsymbol{X}, \boldsymbol{F}, \varphi) \geq a(|\boldsymbol{F}|^p + |\operatorname{cof} \boldsymbol{F}|^q).$$

Then, if $\mathbf{W} \neq \emptyset$, Ψ_S attains its minimum in $\mathbf{W}$.

The law proposed in (10) yields the following potential for the mechanics:

$$\Psi_S(\boldsymbol{F}, \varphi) := \psi_{\text{skel}}(\boldsymbol{F}) + \psi_s(\varphi_s).$$

We note that if ψ_{skel} is polyconvex and ψ_s is convex, then Ψ_S is polyconvex as well, which grants the existence of minimizers for problem (12). We stress that there are no growth conditions for the potential ψ_s with respect to J.

11

Porous media subproblem Under the stated hypotheses, problem (5b) becomes: given $\boldsymbol{F}$, find φ such that

$$\frac{\partial \varphi}{\partial t} - \operatorname{div}\left(\nabla p(\boldsymbol{F}, \varphi)\right) = 0 \quad \text{in} \quad \Omega_0, \tag{14}$$

where $p = \frac{\partial \Psi_P}{\partial \varphi}$ is a given function. Existence of solutions is a consequence of the following result [Váz07], which we have adapted to include the dependence on $\boldsymbol{F}$:

Theorem 2.2 *For each $\boldsymbol{F}$, assume the following hypotheses:*

$(HP)_1$ *The pressure function $\varphi \mapsto p(\boldsymbol{F}, \varphi)$ is continuous and strictly increasing in φ with $p(0) = 0$.*

$(HP)_2$ *The pressure function $\varphi \mapsto p(\boldsymbol{F}, \varphi)$ is smooth with $\frac{\partial p}{\partial \varphi} > 0$ for $\varphi > 0$.*

If the initial data $\varphi(0)$ is such that $\varphi(0) \geq 0, \varphi(0) \in L^1(\Omega_0)$ and $\Psi_P(\boldsymbol{F}, \varphi(0)) \in L^1(\Omega_0)$ for all $\boldsymbol{F}$, then there exists a unique weak solution of problem (14).

The model proposed in (10) yields the porous potential

$$\Psi_P(\boldsymbol{F}, \varphi) \coloneqq \psi_s(\varphi_s) + \psi(\varphi),$$

which is convex in the variable φ if both ψ_s and ψ are convex. In such case, an additional smoothness assumption guarantees that hypotheses $(HP)_1$ and $(HP)_2$ are satisfied, where we observe that the normalization condition in $(HP)_1$ holds due to the consideration of the pre-stress configuration discussed in Section 2.3.

The poromechanics problem Putting the previous theories together, it follows that existence of solutions to problems (14) and (12) (separately) is guaranteed under the following unified hypotheses:

$(H)_1$ ψ_{skel} is a polyconvex and coercive Carathéodory function.

$(H)_2$ ψ_s is a smooth and convex Carathéodory function such that $\psi_s = \infty$ if and only if $J \leq 0$.

$(H)_3$ ψ is a smooth convex function.

$(H)_4$ Ψ_P satisfies the normalization condition $\frac{\partial \Psi_P}{\partial \varphi}(0) = 0$.

Indeed, $(H)_1$ and $(H)_2$ guarantee $(HS)_1, (HS)_2$ and $(HS)_3$; $(H)_2, (H)_3$ and $(H)_4$ instead guarantee $(HP)_1$ and $(HP)_2$. Note also that the convexity of φ_s grants both the convexity of $J \mapsto \psi_s(\varphi_s)$ and $\varphi \mapsto \psi(\varphi_s)$.

This result has two fundamental consequences. From the modeling point of view, it provides useful guidelines for devising the poromechanics potentials proposed in Section 2.2. Most notably, our model is capable of combining the

properties of both physics, meaning the polyconvexity from the mechanics and the convexity from the porous media. In addition, the well-posedness of the sub-problems entails the solvability of the coupled problem by means of an iterative scheme. For instance, this can be achieved by considering a quasi-Newton method where the Jacobian matrix is approximated by its diagonal (or triangular) blocks. In such case, each of the diagonal blocks will be invertible.

3 Mathematical modeling of the epicardial coronary vessels

In this section we present a mathematical model for the epicardial coronary vessels by means of the classic lumped 0D model [QVV16, QMVD19], which is obtained by means of a volumetric averaging of the Navier-Stokes equations in a compliant domain. This approach considers each vessel portion as an independent segment, with pressure and flow as averaged quantities in each segment. The coupling of the segments is done by means of transmission conditions given by mass conservation and pressure continuity. More complex 0D coronary circulation models have been proposed, such as the intramyocardial pump model [SBL81]. However, here we are interested only in a 0D epicardial coronary model, since the intramural vessels are considered through a poroelastic model. To make the model more flexible with respect to the boundary and coupling conditions, we consider the problem variables (volumetric flow and pressure) as being a convex combination of the corresponding proximal and distal quantities.

3.1 Single vessel model

We characterize a single vessel segment with the following parameters: length ℓ, area A, wall thickness H, fluid density ρ_f, Young modulus of the vessel wall E, Poisson ratio of vessel wall ν and fluid viscosity μ_f. The resulting mass and momentum conservation equations for each $t > 0$ are given by [QVV16]

$$L\frac{dQ}{dt} + RQ + P_d - P_p = 0, \tag{15a}$$

$$C\frac{dP}{dt} + Q_d - Q_p = 0, \tag{15b}$$

$$Q(0) = Q_0, \tag{15c}$$

$$P(0) = P_0, \tag{15d}$$

where $R = \frac{K_r \ell}{A^2}, L = \frac{\rho_f \ell}{A}, C = \frac{A^{3/2}\ell}{\eta}$ and $K_r = 8\pi\mu_f, \eta = \frac{\sqrt{\pi}HE}{1-\nu^2}$, with the names R, L, C coming from an analogy with these equations to an RLC circuit. The variables are the volumetric flow rate Q and the mean pressure P, whereas quantities with the subindices d, p stand for distal and proximal variables, see Figure 1 in the Coronaries 0D model frame.

In using this model, it is common practice to approximate the averaged quantities with one of the extremes, for instance $Q \approx Q_d$ and $P \approx P_p$. This procedure results in four different types of well-known segment models, each one corresponding to different combination of boundary conditions[1] on Q (Dirichlet) and P (Neumann). In addition, other types of boundary conditions can be of interest, such as Robin type for which no analogy with an electrical circuit is possible. We propose to consider in each vessel segment two constants α and β in $[0, 1]$ allowing us to interpolate between the distal and proximal quantities and resulting in a generalization of all possible scenarios of boundary conditions:

$$Q = \alpha Q_d + (1 - \alpha)Q_p \quad \text{and} \quad P = \beta P_d + (1 - \beta)P_p.$$

This yields the following modified form of (15a) and (15b):

$$L\frac{d\left(\alpha Q_d + (1 - \alpha)Q_p\right)}{dt} + R(\alpha Q_d + (1 - \alpha)Q_p) + P_d - P_p = 0,$$
$$C\frac{d\left(\beta P_d + (1 - \beta)P_p\right)}{dt} + Q_d - Q_p = 0. \tag{16}$$

Remark 3.1 *If $L = C = 0$, we obtain the well-known Poiseuille flow, which loses dependence on α and β.*

This problem has four unknowns (Q_d, Q_p, P_d, P_p) and so it must be closed with two additional constraints representing the boundary conditions of the starting 3D model. Note that Dirichlet conditions are reduced to fixing Q_d or Q_p (outlet or inlet), whereas Neumann boundary conditions pertain P_d or P_p (outlet or inlet). The proposed model can handle all such scenarios, so in what follows, we consider the model abstractly, with these two extra constraints chosen.

By denoting the unknown as $\boldsymbol{Z} = (Q_d, Q_p, P_d, P_p)^T$, this problem can be rewritten as a differential algebraic equations (DAE):

$$\boldsymbol{E}\dot{\boldsymbol{Z}}(t) + \boldsymbol{H}\boldsymbol{Z}(t) = \boldsymbol{b}(t),$$
$$P(0) = P_0, \tag{17}$$
$$Q(0) = Q_0,$$

where

$$\boldsymbol{E} := \begin{bmatrix} \alpha L & (1-\alpha)L & 0 & 0 \\ 0 & 0 & \beta C & (1-\beta)C \\ 0 & 0 & 0 & 0 \\ 0 & 0 & 0 & 0 \end{bmatrix}, \ \boldsymbol{H} := \begin{bmatrix} \alpha R & (1-\alpha)R & 1 & -1 \\ 1 & -1 & 0 & 0 \\ \gamma_{1qd} & \gamma_{1qp} & \gamma_{1pd} & \gamma_{1pp} \\ \gamma_{2qd} & \gamma_{2qp} & \gamma_{2pd} & \gamma_{2pp} \end{bmatrix}, \ \boldsymbol{b}(t) := \begin{bmatrix} 0 \\ 0 \\ b_3(t) \\ b_4(t) \end{bmatrix}.$$

Constants b_3, b_4 stand for the additional constraints representing the boundary conditions. Regarding the values of γ_{ijk}, we idenify the four classic types of boundary conditions for the starting 3D model according to the distal and proximal conditions:

---

[1]The use of the expression "boundary condition" is widely used in this context. It is of course not a precise notion, as a 0D model has no boundary, but it describes the fact that the conditions required to close the model are given by inlet (proximal) and outlet (distal) quantities, as given for the starting 3D model.

(DD) Dicihlet and Dirichlet,	(ND) Neumann and Dirichlet,
$\gamma_i = \begin{cases} 1 & i \in \{1qd, 2qp\}, \\ 0 & \text{elsewhere.} \end{cases}$	$\gamma_i = \begin{cases} 1 & i \in \{1qd, 2pp\}, \\ 0 & \text{elsewhere.} \end{cases}$
(DN) Dirichlet and Neumann,	(NN) Neumann and Neumann,
$\gamma_i = \begin{cases} 1 & i \in \{1pd, 2qp\}, \\ 0 & \text{elsewhere.} \end{cases}$	$\gamma_i = \begin{cases} 1 & i \in \{1pd, 2pp\}, \\ 0 & \text{elsewhere.} \end{cases}$

In all cases, the existence of a solution of (17) is guaranteed:

Proof. We only show the proof for the **(DD)** case, the others are proved analogously. We use [Cam80, Theorem 3.1.1], so it suffices to show that there exists $s > 0$ such that $(s\boldsymbol{E} + \boldsymbol{H})$ is invertible. Setting $s > 0$ we define

$$\boldsymbol{A} := s\boldsymbol{E} + \boldsymbol{H} = \boldsymbol{E} := \begin{bmatrix} \alpha(R+sL) & (1-\alpha)(R+sL) & 1 & -1 \\ 1 & -1 & s\beta C & s(1-\beta)C \\ 1 & 0 & 0 & 0 \\ 0 & 1 & 0 & 0 \end{bmatrix},$$

and now proceed to obtain $\boldsymbol{Z}$ such that $\boldsymbol{AZ} = \boldsymbol{0}$. In fact, from the last two rows we obtain $Q_d = Q_p = 0$, then the first row gives $P := P_d = P_p$ and finally the second one yields

$$s\beta CP + s(1-\beta)CP = sCP = 0.$$

As $s, C > 0$, we obtain $P = 0$ and thus $\boldsymbol{x} = 0$, which concludes the proof. $\square$

Remark 3.2 *Note that Robin boundary conditions in the 3D model can be easily considered in (17) as linear combinations of $Q_{(\cdot)}$ and $P_{(\cdot)}$. For example, if we denote by $\Omega_{myocardium}$ the domain defined by the myocardium, the interface conditions used in the 3D-0D coupling from [DGFP⁺20] between the lumped FSI model (0D) and the porous media (3D) at the network outlet would be obtained by setting the last equation with $\gamma_{2qd} = \alpha^{-1} > 0, \gamma_{2pd} = 1, \gamma_{2qp} = \gamma_{2pp} = 0, b_4(t) = \frac{1}{|\Omega_{myocardium}|} \int_{\Omega_{myocardium}} p\, dX.$*

3.2 Network of 0D vessels

We now formalize the coupling among consecutive vessel segments, where we note that the resulting structure is that of a forest graph [CCPS09], i.e. the union of connected acyclic undirected graphs. Consider a set of segments $\mathcal{S}$, where we identify each segment by its distal and proximal nodes as $s = \{n_d, n_p\}$. The set of all nodes will be denoted with $\mathcal{N}$, and for a given node $n \in \mathcal{N}$ we consider its inlet and outlet segments, S_n^i and S_n^o respectively. Each segment can be described by Equation (15) with $Q^s = \alpha^s Q_d^s + (1 - \alpha^s)Q_p^s$ (P^s defined
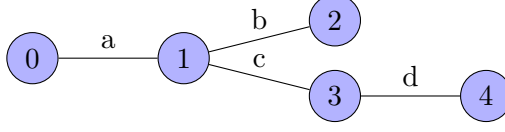
Figure 2: Example network.

analogously), so that the following holds for all $s \in \mathcal{S}$:

$$L^s \frac{dQ^s}{dt} + R^s Q^s + P_d^s - P_p^s = 0,$$

$$C^s \frac{dP^s}{dt} + Q_d^s - Q_p^s = 0,$$ (18)

$$Q^s(0) = Q_0^s,$$

$$P^s(0) = P_0^s.$$

The network begins at its *inflow* segments $\mathcal{S}^{\mathrm{in}}$ and ends at its *outflow* segments $\mathcal{S}^{\mathrm{out}}$, given by

$$\mathcal{S}^{\mathrm{in}} := \{ s \in \mathcal{S} : S_{n_p}^i = \emptyset \}, \quad \text{and} \quad \mathcal{S}^{\mathrm{out}} := \{ s \in \mathcal{S} : S_{n_d}^o = \emptyset \}.$$

For each node $n \in \mathcal{N}$, the interface conditions are given by mass conservation and pressure continuity:

$$\sum_{i \in \mathcal{S}_n^i} Q_d^i = \sum_{j \in \mathcal{S}_n^o} Q_p^j \quad \forall n \in \mathcal{N}, \quad P_d^i = P_p^j \quad \forall i \in \mathcal{S}_n^i, j \in \mathcal{S}_n^o.$$

We consider in practice boundary conditions of type **(NN)** as we impose pressure in both inlets and outlets of the network through $P_p^s = \widehat{P}_{\mathrm{in}}^s \quad \forall s \in \mathcal{S}^{\mathrm{in}}$ and $P_d^s = \widehat{P}_{\mathrm{out}}^s \quad \forall s \in \mathcal{S}^{\mathrm{out}}$. More details on the form of $\widehat{P}_{\mathrm{in}}^s, \widehat{P}_{\mathrm{out}}^s$ will be given in Section 4. For numerical tests regarding the initialization of the model, its conditioning and its dependence on the parameters α and β, see Appendix A.

4   Coupled perfusion problem and solution strategy

In this section we present the coupling between systemic circulation, blood flow in the epicardial coronary vessels and myocardial perfusion. The resulting model can be thought as a sequence of three events:

1. The aortic pressure p_{ao} determines the inlet blood flow in the coronary tree.

2. The blood flows through the epicardial coronaries into the tissue.

3. The blood leaves the tissue through the veins, whose pressure equals p_{veins}.

16

Cardiac perfusion presents very complex spatial interactions. In this regard, a crucial process is the pressure balance between each epicardial coronary vessels and the region it perfuses. To model this, for each epicardial coronary vessel $s \in \mathcal{S}^{\text{out}}$, we associate to its outlet the region Ω_o of the myocardium which should be perfused by it as described in [DGFP$^+$20], referred to as perfusion region [CLM$^+$12, DGFP$^+$20] and such that $\overline{\Omega} = \cup_{o \in \mathcal{S}^{\text{out}}} \overline{\Omega_o}$, see 'Coupling' in Figure 1. Blood flow is connected through each of the aforementioned components as follows:

Inlet pressure We enforce the same pressure at both inlet segments because they stem from the aortic root:

$$P_p^s = p_{\text{ao}} \quad \forall s \in \mathcal{S}^{\text{in}}.$$

Coupling of epicardial coronary vessels with myocardium The outputs of the network representing the epicardial coronary vessels have an assigned pressure equal to the average pressure in the first compartment, i.e.

$$P_d^o = \frac{1}{|\Omega_o|} \int_{\Omega_o} p_1 \, dX \quad \forall o \in \mathcal{S}^{\text{out}}. \tag{19a}$$

The coronaries act on the myocardium through a source term that equals the surface flow on the output. For this, we compute the source term as

$$\theta_1 \Big|_{\Omega_o} = \frac{1}{|\Omega_o|} Q^o = \frac{\alpha^o Q_d^o + (1 - \alpha^o) Q_p^o}{|\Omega_o|}, \quad \forall o \in \mathcal{S}^{\text{out}}. \tag{19b}$$

The venous return The last compartment interacts with the veins through a sink term proportional to their pressure difference:

$$\theta_{N_C} = -\gamma(p_{N_C} - p_{\text{veins}}), \tag{19c}$$

where $\gamma = 10^{-4}$ [MCC$^+$13] and $p_{\text{veins}} = 1 \, \text{kPa}$ [CGSMVC10].

Remark 4.1 *The feedback of the myocardium on the coronaries shown in* (19a) *can generate an artificial pressure gradient between the vessels and the my-ocardium. This can can be alleviated through the Robin condition shown in Remark 3.2*

For the sake of notation, we introduce suitable matrices $\boldsymbol{E}, \boldsymbol{H}$ to rewrite problem (18) in compact form as

$$\boldsymbol{E}\dot{\boldsymbol{Z}} + \boldsymbol{H}\boldsymbol{Z} = \boldsymbol{0}$$

using $\boldsymbol{Z} = (Q_d^1, Q_p^1, P_d^1, P_p^1, ..., Q_d^{|\mathcal{S}|}, Q_p^{|\mathcal{S}|}, P_d^{|\mathcal{S}|}, P_p^{|\mathcal{S}|})$, where $|\mathcal{S}|$ is the cardinality of $\mathcal{S}$. This allows us to write the entire coupled perfusion problem encompassing

problems (18) and (5) together with coupling conditions (19) in weak form as follows: Find $\boldsymbol{y}_s \in L^\infty(0, T; \boldsymbol{H}^1(\Omega))$, $\varphi_i \in L^2(0, T; H^1(\Omega)) \cap C^0([0, T]; L^2(\Omega))$ for $i \in \{1, ..., N_C\}$ and $\boldsymbol{Z} \in C^0([0, T]; \mathbb{R}^{4|\mathcal{S}|})$ such that

$$\int_\Omega (\boldsymbol{P} + \boldsymbol{P}_a(\boldsymbol{F})) : \nabla \boldsymbol{y}_s{}^* \, dX - \int_{\partial\Omega} \boldsymbol{g}(\boldsymbol{y}_s) \cdot \boldsymbol{y}_s{}^* \, dS = 0 \qquad \forall \boldsymbol{y}_s{}^* \in \boldsymbol{H}^1(\Omega),$$

$$\int_\Omega \frac{d\varphi_i}{dt} \varphi_i^* + \boldsymbol{K}_i(\boldsymbol{F}) \nabla p_i \cdot \nabla \varphi_i^* + J \sum_{j=1}^{N_C} \beta_{ij}(p_i - p_j)\varphi_i^* \, dX = \int_\Omega J\theta_i \varphi_i^* \, dX \qquad \forall \varphi_i^* \in H^1(\Omega),$$

$$\boldsymbol{P} = \frac{\partial\Psi}{\partial\boldsymbol{F}}(\boldsymbol{F}, \boldsymbol{\varphi}), \quad p_i = \frac{\partial\Psi}{\partial\varphi_i}(\boldsymbol{F}, \boldsymbol{\varphi}),$$

$$\tag{20a}$$

for all $i \in \{1, ..., N_C\}$ with

$$\theta_i = \begin{cases} \frac{1}{|\Omega_o|}Q^o = \frac{\alpha^o Q_d^o + (1-\alpha^o)Q_p^o}{|\Omega_o|} & i = 1, \forall o \in \mathcal{S}^{\mathrm{out}}, \\ -\gamma(p_{N_C} - p_{\mathrm{veins}}) & i = N_C, \\ 0 & i \in \{1, N_C\}^c \end{cases}$$

and

$$\boldsymbol{E}\dot{\boldsymbol{Z}} + \boldsymbol{H}\boldsymbol{Z} = \boldsymbol{0},$$
$$P_p^i = p_{\mathrm{ao}} \quad \forall i \in \mathcal{S}^{\mathrm{in}},$$
$$P_d^o = \frac{1}{|\Omega_o|} \int_{\Omega_o} p_1 \, dX \quad \forall o \in \mathcal{S}^{\mathrm{out}}.$$
$$\tag{20b}$$

In view of coupling this model with the systemic circulation, we consider aortic and myocardial venous pressures as functions of deformation, which yields $p_{\mathrm{ao}} = p_{\mathrm{ao}}(\boldsymbol{y}_s)$ and $p_{\mathrm{veins}} = p_{\mathrm{veins}}(\boldsymbol{y}_s)$. Models for coupling the aortic pressure to the heart contraction are well established in the literature, and are mainly based on the windkessel model (see [WLW09] for further references). For a complete systemic circulation model coupled with the mechanics, see [RSA$^+$20a, RSA$^+$20b].

4.1 The one-way coupling hypothesis

We propose to neglect the influence of the blood on the tissue, by therefore assuming that $\frac{\partial\Psi}{\partial\boldsymbol{F}} \approx \frac{\partial\psi_{\mathrm{skel}}}{\partial\boldsymbol{F}}$. This is a modeling hypothesis, which allows us to rewrite (5a) as

$$-\operatorname{div}(\boldsymbol{P}(\boldsymbol{F}) + \boldsymbol{P}_a(\boldsymbol{F})) = \boldsymbol{0} \quad \text{in} \quad \Omega_0, \tag{21}$$

where the effect of blood on the mechanics is no longer considered. The perfusion problem under this hypothesis is such that mass conservation (5b) is decoupled from (5a), so we refer to it as the one-way coupling hypothesis. In fact, this is what happens when cardiac displacement is obtained from medical images.

This approach of course neglects the important role of blood pressure during contraction, but it also has several advantages: (i) the computationally expensive electromechanics problem can be solved before the perfusion and quasi-incompressible models already take into account the volume variations of the myocardium due to blood flow, (ii) the incorporation of perfusion into an existing electromechanics software is minimally invasive as it would not require modifying the existing code and (iii) it allows for perfusion to be appended to a cardiac imaging pipeline which obtains displacement tailored to patient-specific data. This last point is fundamental, as it puts into evidence that the use of cardiac deformation obtained from medical images implies modeling assumptions.

4.2 Numerical solver for the one-way coupled model

In this section we propose a numerical strategy for the solution of the proposed perfusion model (20) under the one-way coupling hypothesis. It consists in first performing an entire (electro)mechanics simulation with systemic circulation and then solving the perfusion problem, where the coupling between the porous medium and the epicardial coronary vessels is handled through a fixed point algorithm, which has been tested in the linear setting in [DGFP$^+$20]. For this purpose, we adopt an implicit discretization method (20) with time step Δt. For an arbitrary quantity η, with denote $\eta(t_n) \approx \eta^n$ and define the relevant, discretized in time subproblems as follows.

The epicardial coronary vasculature problem Given $\boldsymbol{\varphi}^{n,k}$ a vector of Lagrangian porosities, find $\boldsymbol{Z}^{n,k+1}$ in $\mathbb{R}^{4|\mathcal{S}|}$ such that

$$
(\boldsymbol{E} + \Delta t(1-\theta)\boldsymbol{H})\boldsymbol{Z}^{n,k+1} = (\boldsymbol{E} - \Delta t\theta\boldsymbol{H})\boldsymbol{Z}^{n-1},
$$
$$
P_p^i = p_{\mathrm{ao}}^n \quad \forall i \in \mathcal{S}^{\mathrm{in}},
$$
$$
P_d^o = \frac{1}{|\Omega_o|}\int_{\Omega_o} p_1(\boldsymbol{F}^n, \boldsymbol{\varphi}^{n,k})\,dX \quad \forall o \in \mathcal{S}^{\mathrm{out}}. \tag{22}
$$

The myocardium problem Given an epicardial coronary vessel solution $\boldsymbol{Z}^{n,k+1}$, find a vector of Lagrangian porosities $\boldsymbol{\varphi}^{n,k+1}$ in $\boldsymbol{H}^1(\Omega)$ such that for all $i \in \{1, ..., N_C\}$ it holds that

$$
\int_{\Omega} \frac{\varphi_i^{n,k+1}}{\Delta t}\varphi_i^* + \boldsymbol{K}_i(\boldsymbol{F}^n)\nabla p_i^n \cdot \nabla\varphi_i^*
$$
$$
+ \sum_{j=1}^{N_C} \beta_{ij}(p_i^n - p_j^n)\varphi_i^*\,dX = \int_{\Omega}\left(J\theta_i(\boldsymbol{Z}^{n,k+1}) + \frac{\varphi_i^{n-1}}{\Delta t}\right)\varphi_i^*\,dX \qquad \forall\varphi_i^* \in H^1(\Omega),
$$
$$
p_i^n = \frac{\partial\Psi}{\partial\varphi_i}(\boldsymbol{F}^n, \boldsymbol{\varphi}^{n,k+1}).
$$
$$
\tag{23}
$$

We write this solution strategy as the pseudo-algorithm shown in Algorithm 3. For the mechanics, we consider the electromechanics model with systemic circulation proposed in [RSA$^+$20a, RSA$^+$20b], whose output is shown in Figure 1 (aortic pressure and PV loop).

Figure 3: Perfusion problem solution algorithm

1: **Input:** Initial displacement $\boldsymbol{y}^0$, Lagrangian porosities $\boldsymbol{\varphi}^0$ and epicardial coronary flow $\boldsymbol{Z}^0$, tolerance `tol` and maximum iterations `maxit`
2: **Mechanics:** Solve (21) to obtain $\boldsymbol{y}^n, p_{\text{ao}}^n, p_{\text{veins}}^n$ for each time step n
3: **Perfusion:**
4: **for** time step $n = 1, ..., T$: **do**
5:    Set `error` $= 1$, `k` $= 0$, $\boldsymbol{Z}^{n,0} = \boldsymbol{Z}^{n-1}$ and $\boldsymbol{\varphi}^{n,0} = \boldsymbol{\varphi}^{n-1}$
6:    **while** `error` $>$ `tol` and `k` $<$ `maxit` **do**
7:       Given $\boldsymbol{\varphi}^{n,k}$, compute $\boldsymbol{Z}^{n,k+1}$ which solves (22)
8:       Given $\boldsymbol{Z}^{n,k+1}$, compute $\boldsymbol{\varphi}^{n,k+1}$ which solves (23)
9:       Update `error` using $\boldsymbol{Z}^{n,k}, \boldsymbol{Z}^{n,k+1}, \boldsymbol{\varphi}^{n,k}, \boldsymbol{\varphi}^{n,k+1}$
10:       `k` $=$ `k` $+ 1$
11:    **end while**
12:    Set $\boldsymbol{Z}^n = \boldsymbol{Z}^{n,k}, \boldsymbol{\varphi}^n = \boldsymbol{\varphi}^{n,k}$
13: **end for**
14: **return** Displacement $\boldsymbol{y}^n$, Lagrangian porosities $\boldsymbol{\varphi}^n$ and epicardial flow $\boldsymbol{Z}^n$ for each time step n

5   Application to the perfusion of the heart

In what follows we present a perfusion model that integrates electromechanics, systemic circulation and myocardial perfusion. More precisely, we consider a simulation of the entire coupled problem (20) on a realistic left ventricle geometry under the one-way coupling hypothesis.

5.1   The anatomical heart model and the physical parameters

The geometry used for simulations is part of the realistic anatomical template developed by the Zygote company [2], from which we extract the left ventricle and the corresponding coronary vessels, meaning that we consider only the vessels which supply the left ventricle. The geometrical properties of the epicardial coronary vessels are extracted using VMTK [ISMA18] and used to formulate the networks. Because of the limited resolution of standard, non invasive imaging techniques, the reconstructed geometry of the coronary tree presents a small number of vessels that initially yields unbalanced perfusion. To alleviate this, we have modified the area of each segment so as to obtain a more homogeneous

---

[2] http://www.zygote.com

inflow. The details about the coronary network setup are provided in Appendix B.

We use the following physical parameters: for the passive mechanics we set $C = 0.88 \cdot 10^3$, $b_f = 8$, $b_s = 6$, $b_n = 3$, $b_{fs} = 12$, $b_{fn} = 3$, $b_{sn} = 3$, $\kappa = 5 \cdot 10^4$ Pa as in [ULM02], while the active mechanics are described through a monodomain equation as in [RSA$^+$20a]; for the myocardial coronary vessels we set $c_{\mathrm{art},1} = 1.333$ Pa, $c_{\mathrm{cap},1} = 22$ Pa, $c_{\mathrm{art},2} = 550$ Pa, $c_{\mathrm{cap},2} = 1009$ Pa, $c_{\mathrm{art},3} = 45$, $c_{\mathrm{cap},3} = 10$, $p_{\mathrm{art,ref}} = 5182.15$ Pa, $p_{\mathrm{cap,ref}} = 2140.32$ Pa as in [BADS88] for the fluid phases and $\kappa_s = 5 \cdot 10^4$ Pa for the solid phase. In the equations, we use $\boldsymbol{K}_{f,\mathrm{art}} = 10^{-9} \mathrm{m}^2(\mathrm{Pa\,s})^{-1}$, $\boldsymbol{K}_{f,\mathrm{cap}} = 10^{-8} \mathrm{m}^2(\mathrm{Pa\,s})^{-1}$, $\beta\mathrm{art,cap} = 3.5 \cdot 10^{-5} \, (\mathrm{Pa\,s})^{-1}$ as in [MCC$^+$13], and finally for the epicardial coronary vessels we set $E = 10^9$ Pa [KNSF13], $\nu = 0.49$ [KSKN16], $H = 10^{-3}$ m [PJC$^+$13] in addition to the well-known $\mu_f = 0.035$ Pa s, $\rho_f = 1060$ kg/m^3 [BM03].

Remark 5.1 *The value $\kappa_s = 5 \cdot 10^4$ is the only parameter that the we have to tune manually. It is set to almost equally balance the quasi-incompressibility constraint enforced on J and φ_s. As detailed in [CM14], it is fundamental that both effects coexist, but a detailed characterization of their interaction remains understudied.*

5.2 Results

The main output of the myocardial perfusion model is shown in Figures 4 and 5. The main quantities of interest are the pressure, the added mass and the coronary flow. In Figure 4 we show the average value of these variables calculated on the ventricle, whereas in Figure 5 we illustrate time snapshots of the entire added mass field in the ventricle. The convergence of the fixed point method is smooth, as it takes no more than 10 iterations to satisfy the tolerance of 10^{-3} with respect to the maximum relative increment between both physics in all of the numerical tests we performed.

Figure 4 aims at illustrating the input-output interactions captured by the proposed model. Panel (a) reports a significant pressure drop along the coronary tree, from the main vessels to the capillaries. The pressure waveform remains anyway almost unperturbed. Without the myocardial contraction, this waveform would propagate also to the added mass and the coronary flow, but as we see from panels (b) and (c), this is not the case. Instead, these results suggest that the heart contraction regulates the perfusion process and in fact the added mass plot in time drops at the systole. In correspondence to the steepest decrease of the added mass, we observe that the flow in the coronaries reaches a minimum, while it increases significantly during the diastole. This effect is called the *systolic impediment* and it is a distinctive trait of blood flow in the myocardium. The ability of the model to capture this effect on the basis of the interaction between aortic pressure and mechanical contraction, without any specific bias that could trigger it, is one of the most relevant outcomes of the presented model. We

further stress that this model was solved by means of our one-way coupling hypothesis, suggesting that the feedback of the blood on the tissue is not essential to reproduce the systolic impediment.

To the best of our knowledge, only [NLL$^+$20] and [CLM$^+$12] propose a myocardial perfusion model coupled with systemic circulation exhibiting the systolic impediment. We note that the model of [CLM$^+$12] considers a flow as input to the coronary vessels, in this way systolic impediment is given externally by the boundary conditions. This is not the case for the one presented in [NLL$^+$20], which has two main differences with respect to ours: (i) incompressibility ($J = 1$) and an ad-hoc relationship for the intra-myocardial pressure depending only on mechanic variables are assumed and (ii) the porous media is replaced by a complex network of vessels reconstructed from morphometric swine measurements representing the entire coronary vasculature (epicardial and myocardial). Our work addresses the problem from the fundamental thermodynamic principles of the physics involved, and in consequence yields comparable results under less hypotheses in a computationally flexible framework.

6   Conclusions

In this work we presented a mathematical model for cardiac perfusion and its coupling with systemic circulation. More precisely, we developed a multi-compartment poromechanics model for the perfusion of the myocardium and a lumped FSI model for the blood flow in the epicardial coronary vessels. The coupling with the systemic circulation was performed through the aortic and myocardial venous pressures. Using a a one-way coupling strategy to solve numerically this coupled problem, we were able to reproduce the systolic impediment, which is a distinctive feature of myocardial perfusion. This result was possible due to the interaction between the pressure in the coronary microvasculature and the aortic pressure, and it shows that the main driver of perfusion is the contraction of the heart. The novel poroelastic potential described in this work considers the fluid porosity in all compartments and quasi-incompressibility for both the geometry and the solid phase. In contrast to other approaches, it has the advantage to ease the computational cost of the problem as it does not require the use of additional multiplier variables. Moreover, it entails the fundamental result that the pressure acting on the myocardial coronary vessels is given by the difference between the intra-myocardial and intra-vascular pressures. We highlight that this is not an ad-hoc choice but a consequence of the considered potential, meaning that our model is thermodynamically consistent. We also devised unified conditions under which the proposed potential guarantees the existence of solutions to both the mechanics and the porous media problems (independently). Besides the analytic relevance of this result, it states that convexity is essential for all of the porous media potentials.
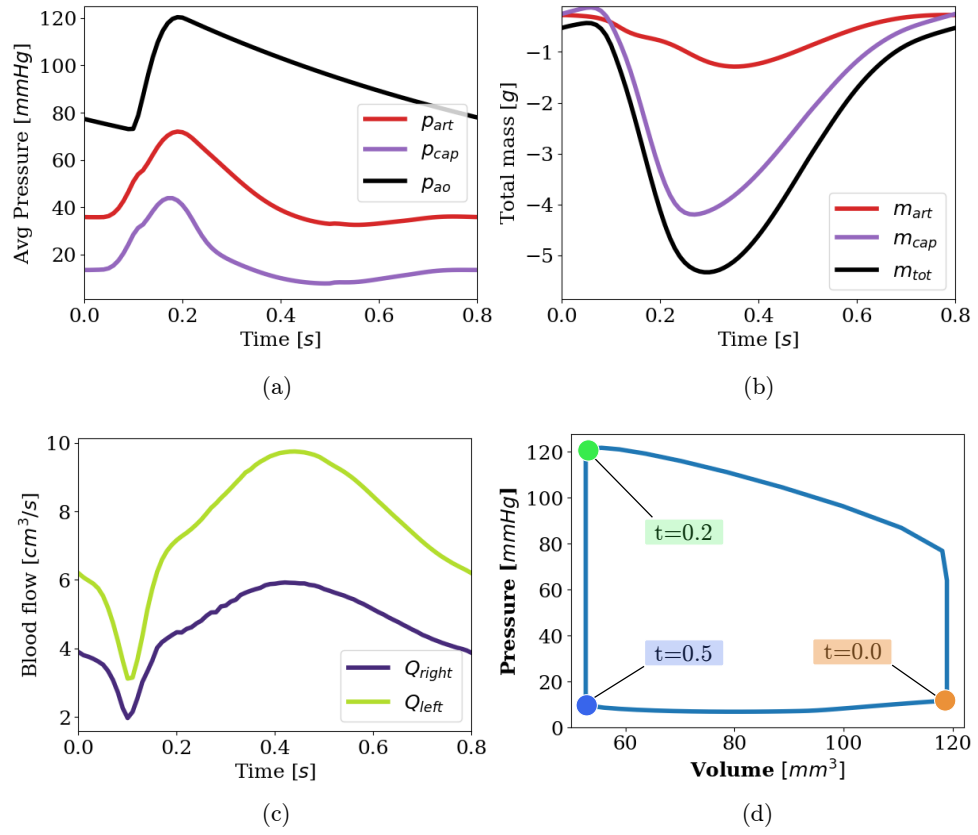
Figure 4: Evolution of global quantities of the myocardial perfusion model: average pressure, total added mass and blood flow, with the PV loop for reference.
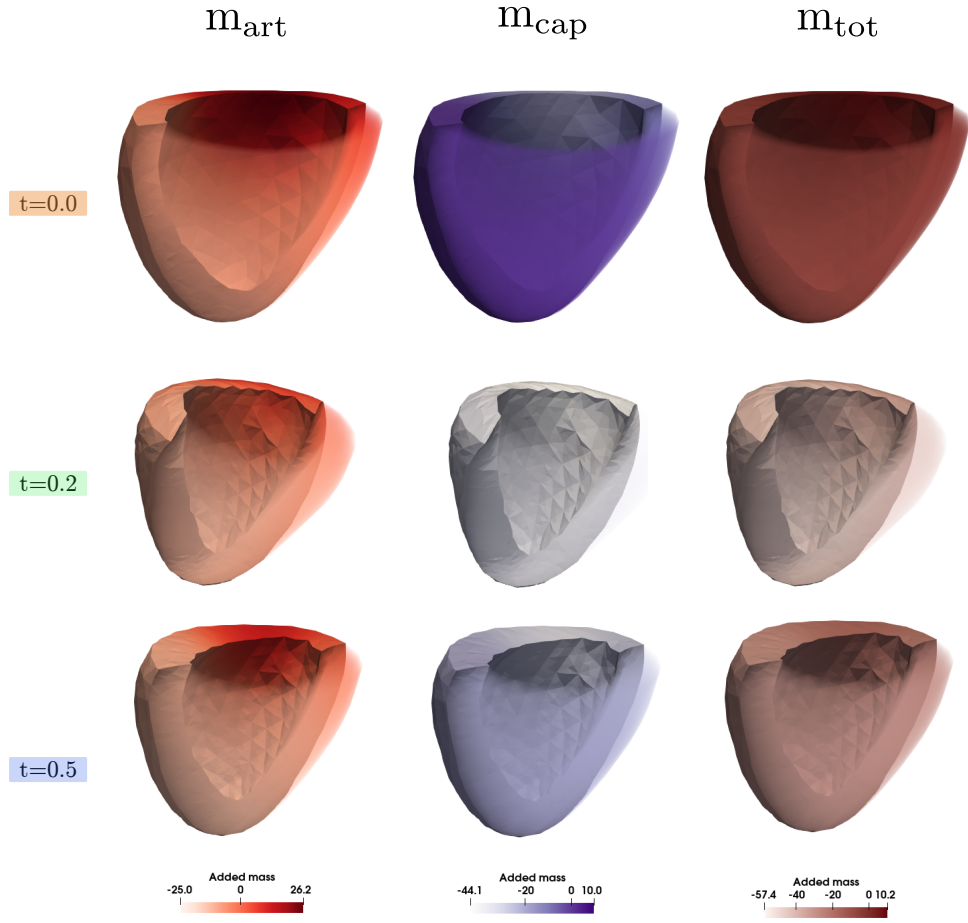
Figure 5: Evolution of the local added masses in arteries and capillaries, together with their global contribution. Chosen instants are shown in the PV loop in Figure 4

Acknowledgements

References

[AANQ11]   D. Ambrosi, G. Arioli, F. Nobile, and A. Quarteroni. Electrome-chanical coupling in cardiac dynamics: the active strain approach. *SIAM Journal on Applied Mathematics*, 71(2):605–621, 2011.

[AKL10a]   D. Algranati, G.S. Kassab, and Y. Lanir. Mechanisms of myocardium-coronary vessel interaction. *American Journal of Physiology - Heart and Circulatory Physiology*, 298(3):H861–H873, 2010.

[AKL10b]   D. Algranati, G.S. Kassab, and Y. Lanir. Mechanisms of myocardium-coronary vessel interaction. *American Journal of Physiology-Heart and Circulatory Physiology*, 298(3):H861–H873, 2010.

[BADS88]   P. Bruinsma, T. Arts, J. Dankelman, and J.A.E. Spaan. Model of the coronary circulation based on pressure dependence of coronary resistance and compliance. *Basic research in cardiology*, 83(5):510–524, 1988.

[BB00]   D.A. Beard and J.B. Bassingthwaighte. The fractal nature of myocardial blood flow emerges from a whole-organ model of arterial network. *Journal of vascular research*, 37(4):282–296, 2000.

[BBPT12]   J.D. Bayer, R.C. Blake, G. Plank, and N.A. Trayanova. A novel rule-based algorithm for assigning myocardial fiber orientation to computational heart models. *Annals of Biomedical Engineering*, 40(10):2243–2254, 2012.

[BCM17]   B. Burtschell, D. Chapelle, and P. Moireau. Effective and energy-preserving time discretization for a general nonlinear poromechanical formulation. *Computers and Structures*, 182:313–324, 2017.

[BF10]   P.J. Blanco and R.A. Feijóo. A 3d-1d-0d computational model for the entire cardiovascular system. *Computational Mechanics, eds. E. Dvorking, M. Goldschmit, M. Storti*, 29:5887–5911, 2010.

[BM03]   O.K. Baskurt and H.J. Meiselman. Blood rheology and hemodynamics. In *Seminars in thrombosis and hemostasis*, volume 29, pages 435–450. Citeseer, 2003.

[Bow80]   R.M. Bowen. Incompressible porous media models by use of the theory of mixtures. *International Journal of Engineering Science*, 18(9):1129–1148, 1980.

[Bow82]   R.M. Bowen. Compressible porous media models by use of the theory of mixtures. *International Journal of Engineering Science*, 20(6):697–735, 1982.

[Cam80]   S. Campbell. *Singular systems of differential equations*, volume 1. Pitman London, 1980.

[CCPS09]   W.J. Cook, W.H. Cunningham, W.R. Pulleyblank, and A. Schrijver. Combinatorial optimization. *Oberwolfach Reports*, 5(4):2875–2942, 2009.

[CGSMVC10] D. Chapelle, J.F. Gerbeau, J. Sainte-Marie, and I.E. Vignon-Clementel. A poroelastic model valid in large strains with applications to perfusion in cardiac modeling. *Computational Mechanics*, 46(1):91–101, 2010.

[CLM+12]   A.N. Cookson, J.J. Lee, C. Michler, R. Chabiniok, E. Hyde, D.A. Nordsletten, M. Sinclair, M. Siebes, and N.P. Smith. A novel porous mechanical framework for modelling the interaction between coronary perfusion and myocardial mechanics. *Journal of biomechanics*, 45(5):850–855, 2012.

[CM14]   D. Chapelle and P. Moireau. General coupling of porous flows and hyperelastic formulations - from thermodynamics principles to energy balance and compatible time schemes. *European Journal of Mechanics, B/Fluids*, 46:82–96, 2014.

[Cou04]   O. Coussy. *Poromechanics*. John Wiley & Sons, 2004.

[CWH+16]   R. Chabiniok, V.Y. Wang, M. Hadjicharalambous, L. Asner, J. Lee, M. Sermesant, E. Kuhl, A.A. Young, P. Moireau, M.P. Nash, D. Chapelle, and D.A. Nordsletten. Multiphysics and multiscale modelling, data–model fusion and integration of organ physiology in the clinic: Ventricular cardiac mechanics. *Interface Focus*, 6(2), 2016.

[dBCD98]   P. de Buhan, X. Chateau, and L. Dormieux. The constitutive equations of finite strain poroelasticity in the light of a micro-macro approach. *European Journal of Mechanics-A/Solids*, 17(6):909–921, 1998.

[DGFP⁺20]   S. Di Gregorio, M. Fedele, G. Pontone, A.F. Corno, P. Zunino, C. Vergara, and A. Quarteroni. A computational model applied to myocardial perfusion in the human heart: from large coronaries to microvasculature. *Journal of Computational Physics*, page 109836, 2020.

[DGQ20]   L. Dede, A. Gerbi, and A. Quarteroni. Segregated algorithms for the numerical simulation of cardiac electromechanics in the left human ventricle. In *The Mathematics of Mechanobiology*, pages 81–116. Springer, 2020.

[DJBBD92]   J.T. Dodge Jr, B.G. Brown, E.L. Bolson, and H.T. Dodge. Lumen diameter of normal human coronary arteries. influence of age, sex, anatomic variation, and left ventricular hypertrophy or dilation. *Circulation*, 86(1):232–246, 1992.

[DK75]   J.M. Downey and E.S. Kirk. Inhibition of coronary blood flow by a vascular waterfall mechanism. *Circulation research*, 36(6):753–760, 1975.

[FAC16]   D.A. Fonseca, P.E. Antunes, and M.D. Cotrim. The morphology, physiology and pathophysiology of coronary microcirculation. *Microcirculation Revisited–From Molecules to Clinical Practice*, pages 15–47, 2016.

[FPS14]   P.C. Franzone, L. Franco Pavarino, and S. Scacchi. *Mathematical cardiac electrophysiology*, volume 13. Springer, 2014.

[FQV09]   L. Formaggia, A. Quarteroni, and A. Veneziani. Multiscale models of the vascular system. In *Cardiovascular mathematics*, pages 395–446. Springer, 2009.

[GDQ19]   A. Gerbi, L. Dedè, and A. Quarteroni. A monolithic algorithm for the simulation of cardiac electromechanics in the human left ventricle. *Mathematics In Engineering*, 1(1):1–37, 2019.

[GMW91]   J.M. Guccione, A.D. McCulloch, and L.K. Waldman. Passive material properties of intact ventricular myocardium determined from a cylindrical model. *Journal of biomechanical engineering*, 113(1):42–55, 1991.

[GPCP90]   C. Guiot, P.G. Pianta, C. Cancelli, and T.J. Pedley. Prediction of coronary blood flow with a numerical model based on collapsible tube dynamics. *American Journal of Physiology-Heart and Circulatory Physiology*, 258(5):H1606–H1614, 1990.

[HAvCR92]   J.M. Huyghe, T. Arts, D.H. van Campen, and R.S. Reneman. Porous medium finite element model of the beating left ventricle. *American Journal of Physiology-Heart and Circulatory Physiology*, 262(4):H1256–H1267, 1992.

[HB11]   M.C. Hsu and Y. Bazilevs. Blood vessel tissue prestress modeling for vascular fluid–structure interaction simulation. *Finite Elements in Analysis and Design*, 47(6):593–599, 2011.

[HBJ$^+$17]   M. Hirschvogel, M. Bassilious, L. Jagschies, S. M Wildhirt, and M.W. Gee. A monolithic 3d-0d coupled closed-loop model of the heart and the vascular system: experiment-based parameter estimation for patient-specific cardiac mechanics. *International journal for numerical methods in biomedical engineering*, 33(8):e2842, 2017.

[HBRS08]   M.R. Hoenig, C. Bianchi, A. Rosenzweig, and F.W. Sellke. The cardiac microvasculature in hypertension, cardiac hypertrophy and diastolic heart failure. *Current vascular pharmacology*, 6(4):292–300, 2008.

[HKL$^+$09]   Y. Huo, B. Kaimovitz, Y. Lanir, T. Wischgoll, J.I.E. Hoffman, and G.S. Kassab. Biophysical model of the spatial heterogeneity of myocardial flow. *Biophysical journal*, 96(10):4035–4043, 2009.

[HS90]   J.I. Hoffman and J.A. Spaan. Pressure-flow relations in coronary circulation. *Physiological Reviews*, 70(2):331–390, 1990.

[ISMA18]   R. Izzo, D. Steinman, S. Manini, and L. Antiga. The vascular modeling toolkit: a python library for the analysis of tubular structures in medical images. *Journal of Open Source Software*, 3(25):745, 2018.

[KCB85]   J.Y. Kresh, M.A. Cobanoglu, and S.K. Brockman. The intramyocardial pressure: a parameter of heart contractility. *The Journal of heart transplantation*, 4(2):241–246, 1985.

[KNSF13]   A. Karimi, M. Navidbakhsh, A. Shojaei, and S. Faghihi. Measurement of the uniaxial mechanical properties of healthy and atherosclerotic human coronary arteries. *Materials Science and Engineering: C*, 33(5):2550–2554, 2013.

[KSKN16]   A. Karimi, T. Sera, S. Kudo, and M. Navidbakhsh. Experimental verification of the healthy and atherosclerotic coronary arteries incompressibility via digital image correlation. *Artery Research*, 16:1–7, 2016.

[KVCC+10]   H.J. Kim, I.E. Vignon-Clementel, J.S. Coogan, C.A. Figueroa, K.E. Jansen, and C.A. Taylor. Patient-specific modeling of blood flow and pressure in human coronary arteries. *Annals of biomedical engineering*, 38(10):3195–3209, 2010.

[LMR+10]   G. Liew, P. Mitchell, E. Rochtchina, T.Y. Wong, W. Hsu, M.L. Lee, A. Wainwright, and J.J. Wang. Fractal analysis of retinal microvasculature and coronary heart disease mortality. *European Heart Journal*, 32(4):422–429, 12 2010.

[LNN+09]   J. Lee, S. Niederer, D. Nordsletten, I. Le Grice, B. Smail, D. Kay, and N.P. Smith. Coupling contraction, excitation, ventricular and coronary blood flow across scale and physics in the heart. *Philosophical Transactions of the Royal Society A: Mathematical, Physical and Engineering Sciences*, 367(1896):2311–2331, 2009.

[LS12]   J. Lee and N.P. Smith. The multi-scale modelling of coronary blood flow. *Annals of biomedical engineering*, 40(11):2399–2413, 2012.

[MCC+13]   C. Michler, A.N. Cookson, R. Chabiniok, E. Hyde, J. Lee, M. Sinclair, T. Sochi, A. Goyal, G. Vigueras, and D.A. Nordsletten. A computationally efficient framework for the simulation of cardiac perfusion using a multi-compartment darcy porous-media flow model. *International journal for numerical methods in biomedical engineering*, 29(2):217–232, 2013.

[MQY94]   S. Müller, T. Qi, and B.S. Yan. On a new class of elastic deformations not allowing for cavitation. In *Annales de l'Institut Henri Poincare (C) Non Linear Analysis*, volume 11, pages 217–243. Elsevier, 1994.

[NKL18]   R. Namani, G.S. Kassab, and Y. Lanir. Morphometric reconstruction of coronary vasculature incorporating uniformity of flow dispersion. *Frontiers in physiology*, 9:1069, 2018.

[NLL+20]   R. Namani, L.C. Lee, Y. Lanir, B. Kaimovitz, S.M. Shavik, and G.S. Kassab. Effects of myocardial function and systemic circulation on regional coronary perfusion. *Journal of Applied Physiology*, 128(5):1106–1122, 2020.

[Oli06]   T.E. Oliphant. *A guide to NumPy*, volume 1. Trelgol Publishing USA, 2006.

[PHW+19]   M.R. Pfaller, J.M. Hörmann, M. Weigl, A. Nagler, R. Chabiniok, C. Bertoglio, and W.A. Wall. The importance of the pericardium for cardiac biomechanics: from physiology to computational modeling. *Biomechanics and modeling in mechanobiology*, 18(2):503–529, 2019.

[PJC+13]   R. Perry, M.X. Joseph, D.P. Chew, P.E. Aylward, and C.G. De Pasquale. Coronary artery wall thickness of the left anterior descending artery using high resolution transthoracic echocardiography–normal range of values. *Echocardiography*, 30(7):759–764, 2013.

[PKJ+20]   L. Papamanolis, H. J. Kim, C. Jaquet, M. Sinclair, M. Schaap, I. Danad, P. van Diemen, P. Knaapen, L. Najman, H. Talbot, C. A. Taylor, and I. Vignon-Clementel. Myocardial perfusion simulation for coronary artery disease: A coupled patient-specific multiscale model. *Annals of Biomedical Engineering*, pages 1–16, 2020.

[QLRRB17]   A.M. Quarteroni, T. Lassila, S. Rossi, and R. Ruiz-Baier. Integrated heart—coupling multiscale and multiphysics models for the simulation of the cardiac function. *Computer Methods in Applied Mechanics and Engineering*, 314:345–407, 2017.

[QMVD19]   A. Quarteroni, A. Manzoni, C. Vergara, and L. Dede'. *Mathematical Modelling of the Human Cardiovascular System: Data, Numerical Approximation, Clinical Applications*, volume 33. Cambridge University Press, 2019.

[QRV01]   A. Quarteroni, S. Ragni, and A. Veneziani. Coupling between lumped and distributed models for blood flow problems. *Computing and Visualization in Science*, 4(2):111–124, 2001.

[QVV16]   A. Quarteroni, A. Veneziani, and C. Vergara. Geometric multiscale modeling of the cardiovascular system, between theory and practice. *Computer Methods in Applied Mechanics and Engineering*, 302:193–252, 2016.

[RSA+20a]   F. Regazzoni, M. Salvador, P.C. Africa, M. Fedele, L. Dede, and A. Quarteroni. A cardiac electromechanics model coupled with a lumped parameters model for closed-loop blood circulation. part I: model derivation. *arXiv e-prints*, 2020.

[RSA+20b]   F. Regazzoni, M. Salvador, P.C. Africa, M. Fedele, L. Dede, and A. Quarteroni. A cardiac electromechanics model coupled with a lumped parameters model for closed-loop blood circulation. part II: numerical approximation. *arXiv e-prints*, 2020.

[SBL81]   J.A. Spaan, N.P. Breuls, and J.D. Laird. Diastolic-systolic coronary flow differences are caused by intramyocardial pump action in the anesthetized dog. *Circulation Research*, 49(3):584–593, 1981.

[Smi04]   N.P. Smith. A computational study of the interaction between coronary blood flow and myocardial mechanics. *Physiological measurement*, 25(4):863, 2004.

[ULM02]   T.P. Usyk, I.J. LeGrice, and A.D. McCulloch. Computational model of three-dimensional cardiac electromechanics. *Computing and Visualization in Science*, 4(4):249–257, Jul 2002.

[Váz07]   J.L. Vázquez. *The Porous Medium Equation: Mathematical Theory.* Oxford University Press, 2007.

[VSW97]   M. A Vis, P. Sipkema, and N. Westerhof. Modeling pressure-flow relations in cardiac muscle in diastole and systole. *American Journal of Physiology-Heart and Circulatory Physiology*, 272(3):H1516–H1526, 1997.

[VYW15]   A.T. Vuong, L. Yoshihara, and W.A. Wall. A general approach for modeling interacting flow through porous media under finite deformations. *Computer Methods in Applied Mechanics and Engineering*, 283:1240–1259, 2015.

[WBDVN69]   N. Westerhof, F. Bosman, C.J. De Vries, and A. Noordergraaf. Analog studies of the human systemic arterial tree. *Journal of biomechanics*, 2(2):121–143, 1969.

[Whi86]   S. Whitaker. Flow in porous media i: A theoretical derivation of darcy's law. *Transport in porous media*, 1(1):3–25, 1986.

[WLW09]   N. Westerhof, J.W. Lankhaar, and B.E. Westerhof. The arterial windkessel. *Medical & biological engineering & computing*, 47(2):131–141, 2009.

[WN11]   H.F. Walker and P. Ni. Anderson acceleration for fixed-point iterations. *SIAM Journal on Numerical Analysis*, 49(4):1715–1735, 2011.

A Numerical tests on the vessel network

In this appendix we numerically study the lumped network model. In particular, we focus on the conditioning of the resulting linear system, its initialization by means of finding a steady state relative to the initial boundary conditions $(\widehat{P}_{\text{in}}^s, \widehat{P}_{\text{out}}^s)$ and its dependence on the parameters α and β. For all tests we consider the bifurcation network from Figure 2 with the parameters described in Section 5.1.

A.1 Problem conditioning

The different scales of the problem parameters can give rise to poor conditioning. In vascular modeling, the area of a coronary is small ($A \approx 10^{-6}\text{m}^2$), which yields large resistance terms $R = O(A^{-2}) \approx 10^{12}$. After discretizing in time, we compute the conditioining number of the resulting matrix with NumPy [Oli06]. To alleviate the bad scaling of the resistance terms, we consider a diagonal preconditioner P which values 1 and R in the rows corresponding to pressure and flow degrees of freedom respectively.

We compute the condition number in the following scenarios: (i) with vs. without diagonal preconditioner $\boldsymbol{P}$, (ii) SI units (m, kg, s, Pa) vs. scaled units (cm, g, s, kPa) and (iii) $\alpha^s = \beta^s = \chi \in \{0, 0.5, 1\}$ for all $s \in \mathcal{S}$. We used the same parameters as the ones used for the complete heart simulation, where the inlet pressure is p_{ao} and the oulet pressure is $9\,\text{kPa}$ in all outlets. The results obtained are shown in Table 1, where we note that the proposed preconditioner works well in all scenarios. The problem in general presents much better conditioning with the scaled units (cm, g, s, kPa), and interestingly, mixing the variables through $\alpha = 0.5$ improves the matrix conditioning.

Scenario	$\chi = 0$	$\chi = 0.5$	$\chi = 1$
No prec, SI	$2.01 \cdot 10^{18}$	$1.29 \cdot 10^{18}$	$1.33 \cdot 10^{18}$
Prec, SI	$3.58 \cdot 10^{12}$	$3.34 \cdot 10^{11}$	$3.91 \cdot 10^{11}$
No prec, scaled	$3.64 \cdot 10^7$	$7.15 \cdot 10^5$	$4.45 \cdot 10^7$
Prec, scaled	$8.27 \cdot 10^6$	$1.63 \cdot 10^5$	$1.01 \cdot 10^7$

Table 1: Condition number for the reduced network models.

A.2 Steady initial conditions

The time-dependence of model (18) is what gives it the ability to incorporate inertia and compliance, but it means that it is sensitive to initial conditions. To obtain realistic initial conditions, we propose performing simulation with the boundary conditions fixed at $t = t_0$ until a steady state is achieved. The

time required to achieve a steady solution can be large, so we additionally use Anderson acceleration [WN11] until a stationary solution is obtained.

A relative tolerance of 10^{-10} on the residual yields the iteration counts shown in Table 2, where the effect of acceleration can be neatly appreciated, yielding an overall iteration count reduction of 75% to 50% for one level of acceleration and roughly 98% for two levels. Three or more levels do not converge, and the two-levels scenario required using a delay of 5 iterations.

# iterations	$\chi = 0$	$\chi = 0.5$	$\chi = 1$
No accel.	4617	4617	4617
Anderson(1)	2172	2336	1075
Anderson(2)	98	75	102

Table 2: Iterations required to achieve a stationary state with and without acceleration for different values of χ and acceleration depths.

A.3 Dependence on α and β

In this section we study the impact that the choice of α and β has on the solution. We consider the inlet pressure profile p_{ao} shown in Figure 1 and an outlet of $9\,kPa$, with all solutions given by the steady dynamic. We show the results of flow and pressure in segment c in Figure 6. The case $\alpha = 0$ yields pressure drops below the outlet pressure with also unrealistic oscillations. Case $\alpha = \beta = \chi = 1$ presents a physiological response and is much stiffer, as seen for example in the minimal difference between distal and proximal flows in all segments. Finally, case $\chi = 0.5$ presents a solution similar to $\chi = 1$, but presents more oscillations. This shows that the latter has the potential to capture more precisely vessel compliance.

B Additional details about the model setup

We used two procedures to balance the areas of the epicardial coronary vessels:

1. An amplifying factor ξ in all areas, so that the new areas are given by $\tilde{A}_s = \xi A_s$ for all segments s. We have found $\xi = 2$ to give realistic results.

2. Use perfusion simulations without deformation, then halved the area of all hyper-perfused terminal vessels and doubled the area of all hipo-perfused vessels until there were no noticeable imperfections in the blood inflow. Whenever doubling/halving proved too coarse, we used the smaller factors x0.75 and x1.5. Results are shown in Table 3.
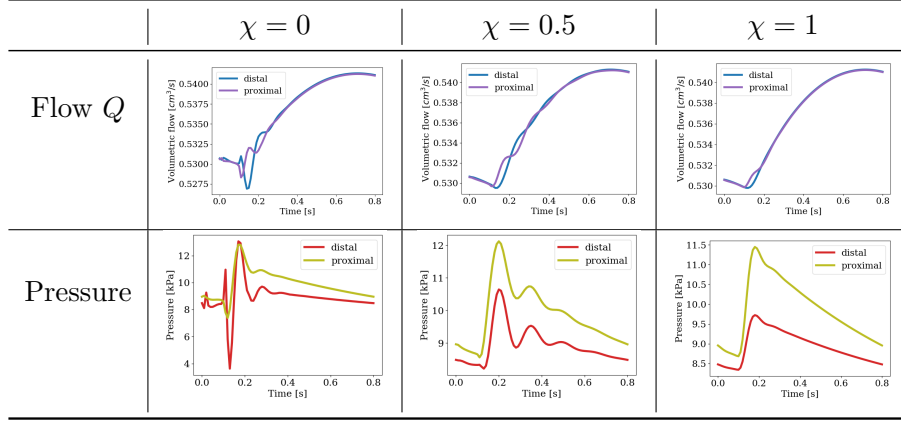
	$\chi = 0$	$\chi = 0.5$	$\chi = 1$
Flow Q			
Pressure			

Figure 6: Flow and pressure for mixing sensitivity test in segment 'c'.

	2	3	4	6	7	8	9	10	16	17	19	20
Original	0.77	0.52	1.23	0.86	1.43	1.79	2.25	1.49	0.92	0.94	0.52	0.5
Modified	0.77	1.32	1.23	0.86	0.22	1.79	4.51	2.96	1.844	2.99	0.52	0.75

	21	22	23	24	25	26	28	29	30	32	33	34
Original	0.50	1.02	6.49	3.79	3.74	3.58	4.09	2.34	1.95	2.59	1.74	1.57
Modified	0.50	1.02	6.49	3.79	3.74	3.58	4.09	2.34	1.95	1.3	1.045	1.50

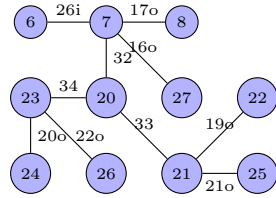Table 3: Modified vessel areas for Zygote coronaries in $10^{-6}\, m^2$.

Also, the spatial heterogeneity of source terms given by the perfusion regions generates numerical instabilities due to the reaction term coming from the compartments interaction, for which we enlarged the permeability tensors to 10^{-7}.
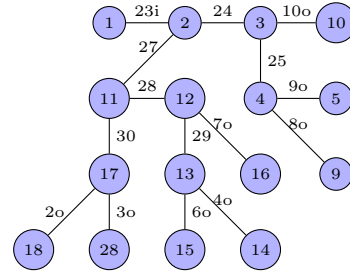
(a) Zygote left coronaries.
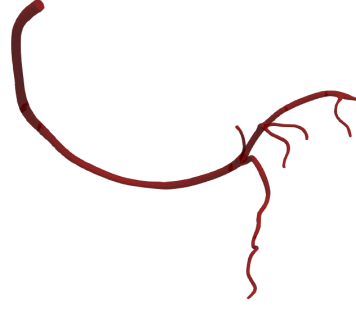
(b) Zygote right coronaries.

(c) Reduced model and tags of left coronaries.

(d) Reduced model and tags of right coronaries.

Figure 7: Left coronary tree model reduction. Inlet and outlet segments denoted with 'i' and 'o' respectively.

MOX Technical Reports, last issues

Dipartimento di Matematica
Politecnico di Milano, Via Bonardi 9 - 20133 Milano (Italy)

38/2021   Giusteri, G. G.; Miglio, E.; Parolini, N.; Penati, M.; Zambetti, R.
Simulation of viscoelastic Cosserat rods based on the geometrically exact dynamics of special Euclidean strands

36/2021   Parolini, N.; Dede', L; Antonietti, P. F.; Ardenghi, G.; Manzoni, A.; Miglio, E.; Pugliese, A.; V
SUIHTER: A new mathematical model for COVID-19. Application to the analysis of the second epidemic outbreak in Italy

37/2021   Dassi, F.; Fumagalli, A.; Mazzieri, I.; Scotti, A.; Vacca, G.
A Virtual Element Method for the wave equation on curved edges in two dimensions

34/2021   Bonaventura, L.; Gatti F.; Menafoglio A.; Rossi D.; Brambilla D.; Papini M.; Longoni L.
An efficient and robust soil erosion model at the basin scale

35/2021   Regazzoni, F.; Quarteroni, A.
Accelerating the convergence to a limit cycle in 3D cardiac electromechanical simulations through a data-driven 0D emulator

33/2021   Lupo Pasini, M.; Gabbi, V.; Yin, J.; Perotto, S.; Laanait, N.
Scalable balanced training of conditional generative adversarial neural networks on image data

32/2021   Sangalli, L.M.
Spatial regression with partial differential equation regularization

31/2021   Ferraccioli, F.; Arnone, E.; Finos, L.; Ramsay, J.O.; Sangalli, L.M.
Nonparametric density estimation over complicated domains

30/2021   Fumagalli, I.
A reduced 3D-0D FSI model of the aortic valve including leaflets curvature

29/2021   Fumagalli, I.; Vitullo, P.; Scrofani, R.; Vergara, C.
Image-based computational hemodynamics analysis of systolic obstruction in hypertrophic cardiomyopathy